

# Impact crater related surficial deposits on Venus: Multipolarization radar observations with Arecibo

Lynn M. Carter

Department of Astronomy, Cornell University, Ithaca, New York, USA

Donald B. Campbell

Department of Astronomy and the National Astronomy and Ionosphere Center, Cornell University, Ithaca, New York, USA

Bruce A. Campbell

Center for Earth and Planetary Studies, National Air and Space Museum, Smithsonian Institution, Washington, D. C., USA

Received 19 December 2003; revised 12 April 2004; accepted 28 April 2004; published 22 June 2004.

[1] The distribution of surficial deposits in the vicinity of impact craters on Venus was studied using measurements of the polarization properties of the reflected radar wave. Subsurface scattering of an incident circularly polarized radar signal results in a linearly polarized component in the radar echo due to the differing transmission coefficients at a smooth (at wavelength scales) atmosphere-surface boundary for the horizontal (H) and vertical (V) linearly polarized components of the incident wave. Arecibo 12.6 cm wavelength radar observations in 1999 and 2001 provided images of the surface of Venus in the full Stokes polarization parameters of the reflected echo, from which images in the degree of linear polarization were derived. These images show that substantial areas of Sedna, Guinevere, and Lavinia Planitias return a radar echo with a significant degree of linear polarization, indicating that mantling deposits may be relatively widespread on the plains of Venus. The areas showing linear polarization enhancements are strongly correlated with topographic features, primarily impact craters, dome fields, and windblown deposits, including dune fields. A strong linearly polarized echo component ( $\sim 10\text{--}40\%$  linear polarization) is found from regions near 45 impact craters, including 5 parabolas. These linear polarization features typically correspond to diffuse, higher backscatter cross-section (bright) regions in Magellan images. The linearly polarized component in these regions is attributed to subsurface echoes from a mantled substrate or from buried rocks.

*INDEX TERMS:* 6295 Planetology: Solar System Objects: Venus; 5420 Planetology: Solid Surface Planets: Impact phenomena (includes cratering); 5470 Planetology: Solid Surface Planets: Surface materials and properties; 5464 Planetology: Solid Surface Planets: Remote sensing; 6949 Radio Science: Radar astronomy; *KEYWORDS:* impact craters, radar, surface properties, Venus

**Citation:** Carter, L. M., D. B. Campbell, and B. A. Campbell (2004), Impact crater related surficial deposits on Venus: Multipolarization radar observations with Arecibo, *J. Geophys. Res.*, 109, E06009, doi:10.1029/2003JE002227.

## 1. Introduction

[2] The surface of Venus has around 1000 impact craters that are distributed uniformly over the surface of the planet [Schaber *et al.*, 1992; Phillips *et al.*, 1992]. Many of these craters have associated deposits that show up clearly in Magellan radar images; for example, 60 of the craters have parabola-shaped deposits that open toward the west and can be thousands of kilometers in length [D. B. Campbell *et al.*, 1992; Schaller and Melosh, 1998; Basilevsky and Head, 2002]. While most of the parabolas have a low backscatter cross section (are dark) in the Magellan Synthetic Aperture Radar (SAR) images, some are bright, or have an interior

bright parabola [D. B. Campbell *et al.*, 1992]. The dark deposits are generally taken to be a fine-grained (pebble-sized and smaller) material that mantles the underlying surface and reduces radar backscattering. The bright deposits are thought to be rougher, with surface roughness scales of centimeters or larger. D. B. Campbell *et al.* [1992] also identified nine large circular dark features, 300 to 2000 km in size, which may be degraded parabolas [Herrick *et al.*, 1997].

[3] Besides the parabola deposits, many craters (including many of those with parabolas) have a nearly circular radar dark halo, tens of kilometers in radius. The halos are inferred to be smooth surfaces produced as part of the impact process, and there are several theories regarding their formation [Phillips *et al.*, 1992; McKinnon *et al.*, 1997]. One possibility is that the atmospheric shock wave

associated with the bolide pulverizes the surface which creates a layer of fine-grained (radar-dark) debris [Phillips *et al.*, 1992]. It has also been suggested that the halos are depositional in nature, formed by the rainout of impact ejecta [Phillips *et al.*, 1992; Schultz, 1992]. In some cases there is no crater at all, only a dark splotch presumably created when an impactor disintegrated before hitting the surface.

[4] Crater-related deposits, and inferred changes in their properties with time, have been used to develop methods for estimating the relative ages of large areas of Venus. Such approaches are necessary because the global population of craters does not support statistically robust age dating, as is possible for other planetary surfaces (e.g., the Moon, Mars). Examination of the terrain surrounding the parabolic deposits indicates that they are some of the youngest features on Venus, and it has been proposed that all impacts large enough to form craters with a diameter greater than  $\sim 20$  km result in parabolas which are subsequently weathered away [D. B. Campbell *et al.*, 1992; Schaller and Melosh, 1998]. The parabolas are useful for relative dating since they form quickly and cover large areas of the surface. Since only about 10% of craters have parabolas, weathering processes must operate fairly quickly to modify the surface and remove the SAR signature [D. B. Campbell *et al.*, 1992; Izenberg *et al.*, 1994].

[5] Radar has also been used for remote sensing of impact crater sites on Earth. McHone *et al.* [2002] used the Space Radar Laboratory (SRL) to image terrestrial impact structures and compared these data to aerial photos. Several craters were imaged at L band (24 cm), C band (5.6 cm), and X band (3 cm), mostly in Australia and northern Africa. The radar was often able to reveal buried parts of the crater rim or show that the crater had a larger ejecta blanket than was measured from optical observation. In radar images of craters filled with windblown sand or with playa material, the smooth deposits produce a radar dark crater floor that allows the rougher radar-bright crater rim to stand out [McHone *et al.*, 2002].

[6] Since both are radar-dark, thin surface mantling layers are not readily discriminated from bare, smooth terrain in Magellan images. While Magellan emissivity data can provide evidence for lower bulk densities in areas of fine debris cover, these data are also affected by the roughness and dielectric constant of the surface materials [Campbell, 1994; Pettengill *et al.*, 1992]. The linear polarization analysis presented below provides an independent assessment of surficial layers. This type of multipolarization radar analysis has been used before to study the Moon. In the 1960's, radar measurements of the Moon in two orthogonal linear polarizations led to models for near-surface properties of the lunar regolith [Hagfors and Evans, 1968]. Dual-polarization radar data at 3 cm wavelength have been used to measure the scattering properties of the lunar surface near impact craters [B. A. Campbell *et al.*, 1988, 1992]. Stacy [1993] created 12.6 cm wavelength multipolarization radar maps of the lunar poles and several mare areas including Sinus Iridium and part of Mare Imbrium. The fraction of linearly polarized echo power was compared to predictions for surface scattering, showing that some of the scattering in mare regions must come from subsurface quasi-specular (or mirror-like) scattering. In this paper, we apply a similar

multipolarization radar technique to characterize subsurface scattering associated with crater ejecta on Venus.

## 2. Arecibo Radar Observations

[7] We used the Arecibo Observatory S band (12.6 cm) radar system for delay-Doppler mapping of Venus during two inferior conjunctions; August 1999 and March 2001. The subradar point changed between the two conjunctions, from  $8.8^\circ\text{N}$ ,  $\sim 332^\circ\text{E}$  in 1999 to  $9.5^\circ\text{S}$ ,  $\sim 338^\circ\text{E}$  in 2001. A right circularly polarized wave was transmitted, and we received both right and left circular polarizations. The beamwidth of the Arecibo telescope at 12.6 cm is two arcminutes, approximately twice the angular diameter of Venus at inferior conjunction. The resulting delay-Doppler north-south ambiguity problem was reduced by pointing north and south of the planet on alternate runs so that the beam of the telescope would preferentially illuminate one hemisphere. (A run is one transmit and receive cycle, lasting about 10 minutes for the Venus observations.) The beam was offset by  $\sim 0.75$  arcminute when transmitting and  $\sim 1$  arcminute when receiving. Although it is theoretically possible to separate the contributions from each hemisphere by modeling the telescope gain, in practice this process significantly reduced the signal-to-noise ratio and therefore compromised the linear polarization analysis. This means that our maps are still partially ambiguous, especially near the equator, despite the asymmetric illumination by the radar.

[8] In 1999 we used a phase coded radar signal with a basic time resolution of  $4.2 \mu\text{s}$ , which corresponds to a range resolution of 0.63 km. We found that we needed significant averaging in spatial resolution to achieve a good signal-to-noise for the polarization results, so in 2001 we used a time resolution of  $8.0 \mu\text{s}$  to obtain a range resolution of approximately 1.2 km. At an incidence angle of  $45^\circ$  the surface resolutions are 0.89 km and 1.7 km, respectively.

[9] For each run we created complex-valued delay-Doppler images for both received circular polarizations. During the delay-Doppler mapping process, we rotated the data to correct for parallactic angle changes as the altitude-azimuth telescope tracked Venus. We then combined the two circular polarizations to form delay-Doppler images for each of the four Stokes polarization parameters. The Stokes parameters can be used to completely describe the polarization state of a wave [Jackson, 1999]. When the electric fields are defined in terms of orthogonal circular polarizations, the Stokes parameters are given by

$$S = \begin{bmatrix} S_1 \\ S_2 \\ S_3 \\ S_4 \end{bmatrix} = \begin{bmatrix} \langle |E_L|^2 \rangle + \langle |E_R|^2 \rangle \\ 2\Re\langle E_L E_R^* \rangle \\ 2\Im\langle E_L E_R^* \rangle \\ \langle |E_L|^2 \rangle - \langle |E_R|^2 \rangle \end{bmatrix} \quad (1)$$

where  $E_L$  and  $E_R$  are the fields for the left and right circular polarizations respectively. The first Stokes parameter ( $S_1$ ) is a measure of the total average power. The second and third Stokes parameters ( $S_2$  and  $S_3$ ) describe the linear polarization state of the wave, and the fourth Stokes parameter ( $S_4$ )

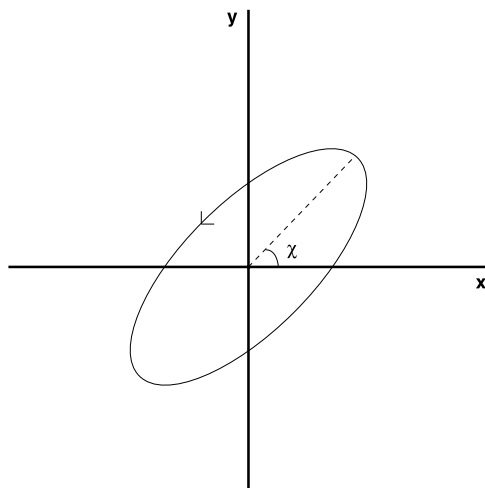


**Figure 1.** A diagram of the polarization ellipse for a wave traveling out of the page, showing the polarization angle,  $\chi$ .

is related to the magnitude and handedness of circular polarization.

[10] For purely a right circularly polarized transmitted wave,  $S_1 = \langle |E_R|^2 \rangle$  and  $S_2$  and  $S_3$  are zero because  $E_L$  is zero. Therefore the transmitted signal has no linearly polarized component. However, while there is no net linearly polarized transmitted power, the incident circularly polarized wave can be thought of as the combination of two linearly polarized waves, one parallel to the plane of incidence (V-polarized) and one perpendicular to the plane of incidence (H-polarized). If there is a subsurface reflection, the backscattered echo power will be partially linearly polarized because the transmission coefficients into and out of the surface are different for the V and H components. The received echo will have a degree of linear polarization that can be defined as

$$m_l = \frac{\sqrt{S_2^2 + S_3^2}}{S_1} \quad (2)$$

Conversely, if there is no contribution to the echo power from subsurface reflections then the linearly polarized Stokes parameters ( $S_2$  and  $S_3$ ) are expected to be zero. Unusual surface geometries that allow multiple-bounce reflections can also create non-zero values for  $S_2$  and  $S_3$ , as can long narrow linear surface structures [B. A. Campbell *et al.*, 1988, 1992; Stacy, 1993]. However, such geometries should occur only in localized regions, not over a significant fraction of our total mapped area.

[11] The polarization state of the reflected wave can be represented as an ellipse, where the long axis of the ellipse indicates the direction of the linear polarization. The orientation of the polarization ellipse will be parallel to the plane of incidence and reflection and will change as this plane rotates across the planet's surface. The angle of the long axis of this ellipse is calculated from

$$\chi = \frac{1}{2} \arctan\left(\frac{S_3}{S_2}\right) \quad (3)$$

Figure 1 shows a diagram of the polarization ellipse and polarization angle. For the unusual surface geometries

discussed above, the polarization angle will appear rotated relative to what is expected from subsurface scattering.

[12] We processed each year and hemisphere separately to produce four maps of the degree of linear polarization. The individual Stokes-parameter images of Venus were mapped into a Mercator projection and spatially averaged. Runs from three days of observing were combined and maps of the degree of linear polarization ( $m_l$ ) were formed from the Stokes parameter images. The final 1999 maps have a resolution of 16 kilometers. The northern hemisphere map is a combination of 13 runs, and the southern hemisphere map is a combination of 11 runs. The final 2001 maps have a resolution of 12 kilometers, and the northern hemisphere consists of 17 runs while the southern hemisphere consists of 15. An example of these maps is shown in Figure 2. We also created maps of the total power ( $S_1$ ) and of the relative polarization angle ( $\chi$ ) at the same resolution.

[13] In the following sections, we compare our maps of the degree of linear polarization with the Arecibo total power images and Magellan data to link areas of apparent subsurface scattering with geologic features. To facilitate this comparison, we created color overlays where the value of each pixel is the Magellan SAR image value, and the hue of each pixel is determined by the linear polarization color scale. Overlays for seven craters are shown in Figure 3. The polarization data were smoothed before they were combined with the SAR images, so the resolutions of the overlays are lower than the maps discussed above. Our data registers with the Magellan data to within a few kilometers, or less than a pixel in the spatially averaged data. The offset comes from ephemeris errors that are incorporated into the delay-Doppler to latitude-longitude conversion. It was measured using the craters Ariadne, Carson, Stuart and Aurelia as references.

[14] Instrumental cross coupling between the circular polarizations and statistical fluctuations in the  $S_2$  and  $S_3$  images can both produce a spurious degree of linear polarization. Since the echo near the subradar point is dominated by mirror-like reflections that generate a left circularly polarized echo (for a right circularly polarized incident wave), measuring the ratio of the two circular polarizations at near normal incidence gives an upper limit on the errors induced by cross coupling. For both epochs of Venus observations, the power measured near the subradar point in the right circular polarization is about 600 times below that in the left circular polarization, which leads to errors in  $m_l$  of 4%. For a degree of linear polarization measurement of 0.35, this contributes an error of 0.01. The  $S_2$  and  $S_3$  images have statistical noise which is squared to produce a non-zero value of  $m_l$  even if there is no linearly polarized echo component [Hagfors and Campbell, 1974]. These errors are significantly reduced by spatial averaging, and so this also has a small effect on our final degree of linear polarization maps. The predicted false degree of linear generated by these statistical errors is 0.02 near the subradar point and 0.04 at incidence angles of  $70^\circ$ .

[15] An additional source of error is introduced into the data when the background noise level of the total power ( $S_1$ ) image is subtracted. There was about a 6% statistical fluctuation in the average noise value measured for each run; for a degree of linear polarization value of 0.35 this contributes an error of 0.02 to the measured values of  $m_l$ . If

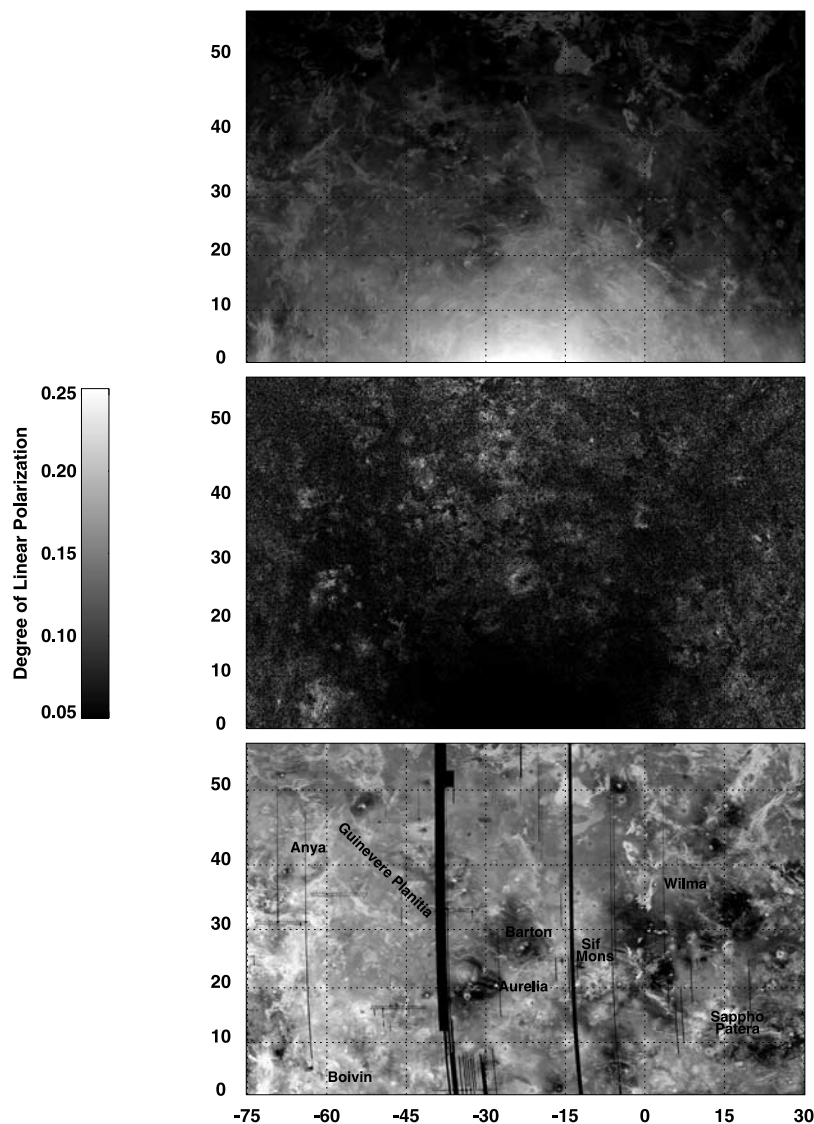


**Figure 2.** (top) An Arecibo Mercator projection map of the northern hemisphere of Venus, showing the total power ( $S_1$ ). The highest power echoes occur at the lower center of the map, where there are strong specular reflections from areas near the subradar point. (middle) The corresponding map of the degree of linear polarization. Both maps were created from the data taken in 2001. (bottom) A Magellan SAR image of the same area with surface features labeled.

the noise was oversubtracted, the total power would be close to zero in places with a low backscatter cross section, and the degree of linear polarization would be unrealistically large. This only occurs in regions with a very low backscatter cross-section that are at high incidence angles (e.g., Lakshmi Planum), and such areas were not considered in our analysis. For a degree of linear polarization value of 0.35 at an incidence angle of  $45^\circ$  the minimum total error (combining only the errors discussed above) is about 0.04. For a  $m_l$  value of 0.15 at  $45^\circ$  incidence, the total error is 0.03.

### 3. Physical Interpretation of Multipolarization Radar Measurements

[16] Radar scattering from planetary surfaces is, in general, a mixture of quasi-specular and diffuse scattering.

Quasi-specular scattering will generate an echo with a clear polarization signature; for a right circularly polarized incident wave the specular echo from the surface-atmosphere boundary will be left circularly polarized. Diffuse scattering from wavelength scale structures will tend to randomize the polarization. As discussed in section 2, a circularly polarized wave can be represented as a combination of two linear (H and V) components. This wave will refract into a surface that is smooth at wavelength scales, and if it is reflected from embedded rocks or from an underlying surface with a higher dielectric constant, then the resultant echo will have a linearly polarized component. This linear polarization arises from the different H and V transmission coefficients into and out of the smooth surface.

[17] A diagram illustrating scattering from a rough, sub-surface layer is shown in Figure 4. The mantling layer has a dielectric constant and loss tangent that depend on its

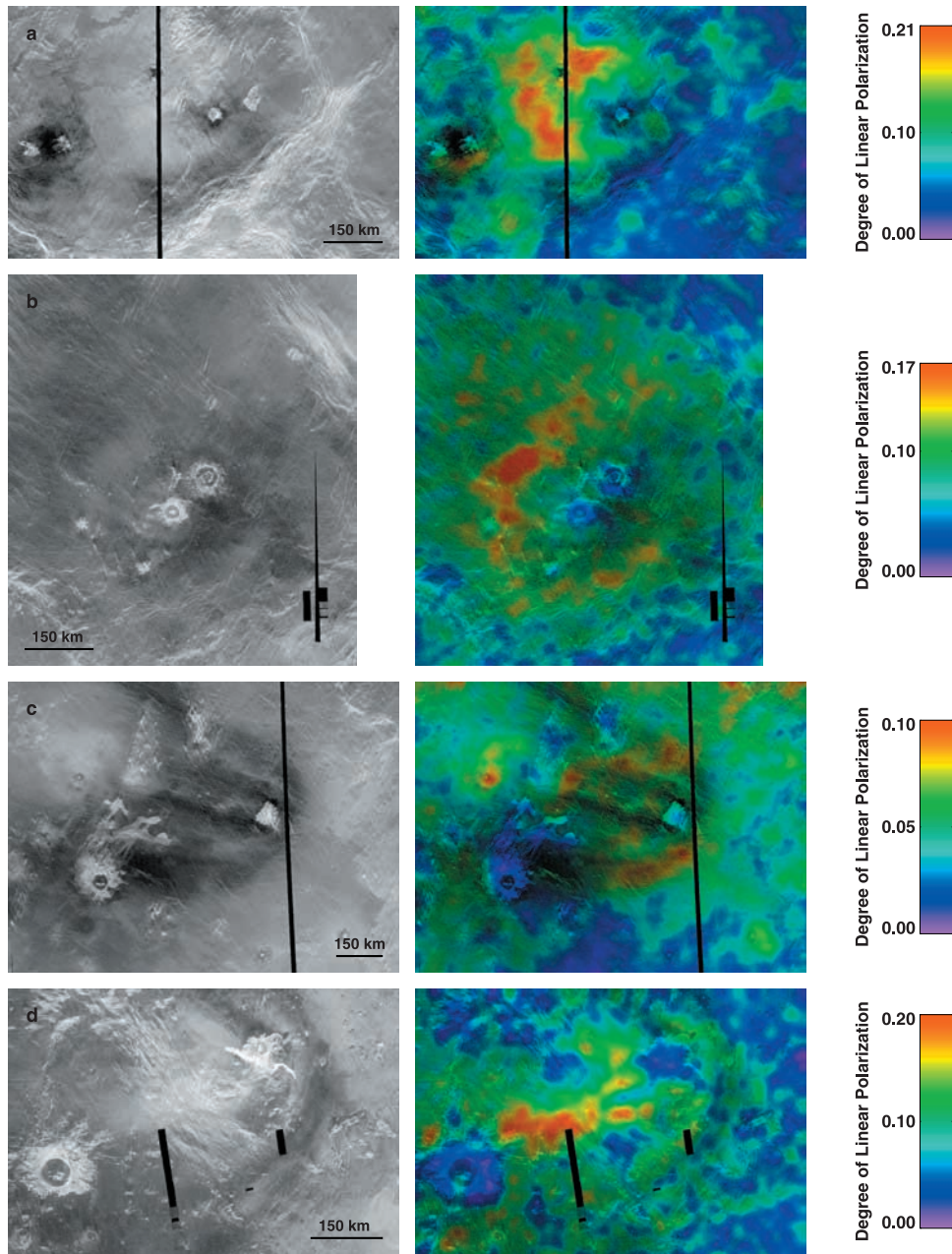


**Figure 3.** Color overlays produced by combining the Arecibo degree of linear polarization maps with Magellan SAR images. The SAR images used to create the overlays are shown on the left for comparison. The degree of linear polarization overlays have been smoothed in order to reduce the sharp “pixellated” look and stretched to a color scale to give the best display for each crater. Color bars giving the range of degree of linear polarization values are shown for each crater. The craters shown are (a) Anya, (b) Barton, (c) Aurelia, (d) Carson, (e) Xantippe, (f) Neliike, and (g) Stuart.

composition and porosity [Campbell and Ulrichs, 1969]. When the radar wave travels from the atmosphere into the surface, it is refracted according to Snell’s Law, resulting in a lower angle of incidence onto any subsurface layer. The Fresnel power transmission coefficients for the H and V components of the wave are [Jackson, 1999]

$$T_H(\theta, \epsilon') = \frac{4 \cos \theta \sqrt{\epsilon' - \sin^2 \theta}}{(\cos \theta + \sqrt{\epsilon' - \sin^2 \theta})^2} \quad (4)$$

$$T_V(\theta, \epsilon') = \frac{4 \epsilon' \cos \theta \sqrt{\epsilon' - \sin^2 \theta}}{(\epsilon' \cos \theta + \sqrt{\epsilon' - \sin^2 \theta})^2} \quad (5)$$

where  $\epsilon'$  is the real part of the surface dielectric constant ( $\epsilon = \epsilon' + i\epsilon''$ ) and  $\theta$  is the incidence angle. When a circularly polarized wave propagates into the surface, the V component of the wave is preferentially transmitted, changing the wave polarization from circular to elliptical.

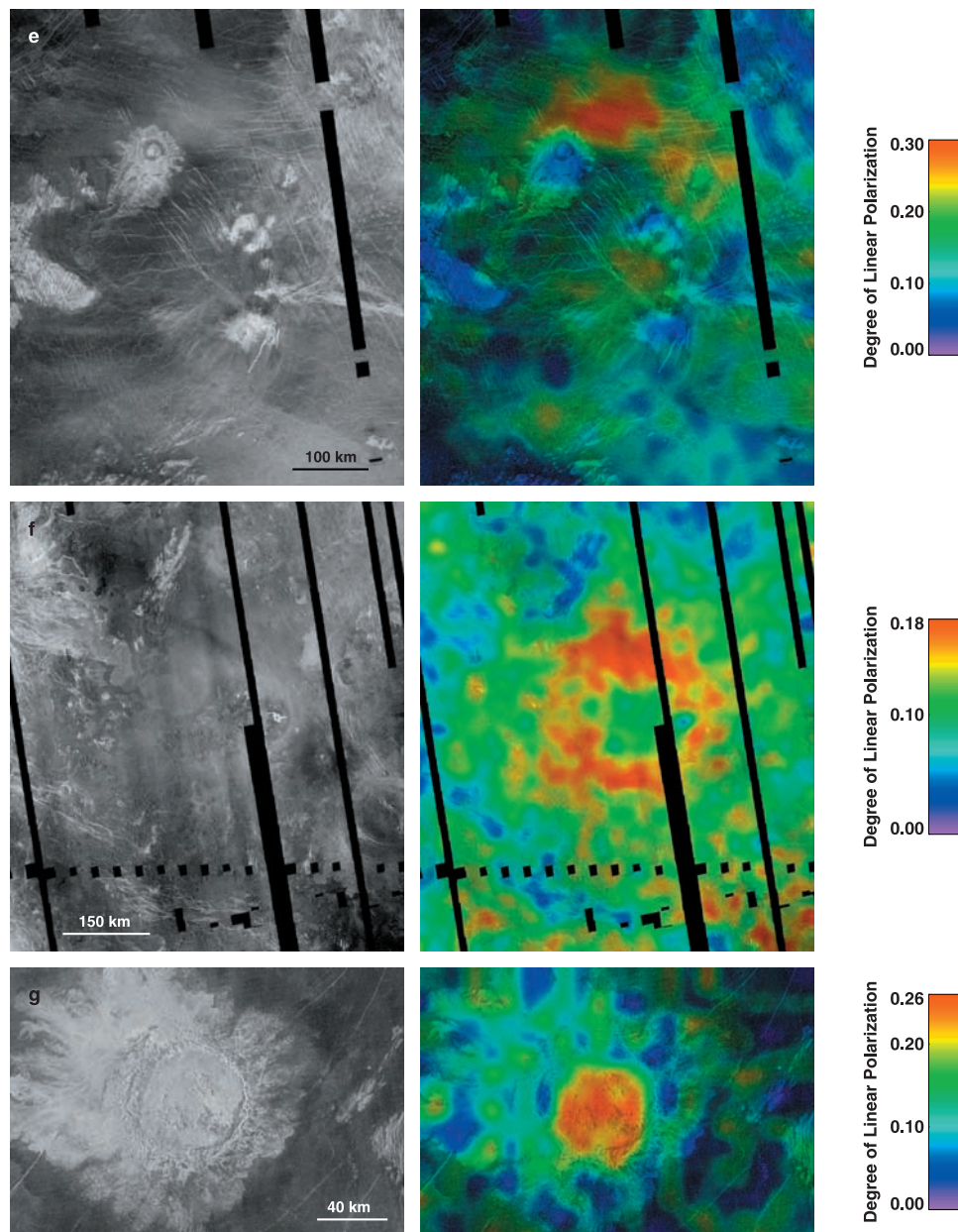


**Figure 3.** (continued)

[18] The magnitude of the linearly polarized component of the backscattered echo power depends on the specific combination of surface and subsurface scattering that occurs over a given resolution cell. It is useful to first consider the degree of linear polarization predicted by the simplest model: a gently undulating, mantled terrain characterized by strictly quasi-specular reflections. In this case, it is assumed that all the received power comes from the component of the incident wave that travels into the surface, reflects quasi-specularly from the subsurface structure, and exits the surface to return to the radar. Both the numerator and denominator of  $m_l$  then depend on the same value of the subsurface reflection coefficient which cancels to leave an expression for  $m_l$  that depends solely on the transmission coefficients for the surface-atmosphere interface. Figure 5 is a graph of the relationship between the degree of linear

polarization, incidence angle, and dielectric constant for this model. At normal incidence, the degree of linear polarization is zero, and it increases as the incidence angle increases. In addition, larger surface dielectric constants will give a higher degree of linear polarization.

[19] Although this model demonstrates some basic trends, most mantled surfaces will be more complex and the values of  $m_l$  will differ from those shown in Figure 5. The subsurface reflectors may be buried rocks instead of a buried planar substrate. If the subsurface reflection is characterized by diffuse scattering from wavelength-scale structures, the measured degree of linear polarization will be smaller. The measured value of  $m_l$  will also decrease with increasing reflections from the upper surface of a mantling layer. A very rough upper surface effectively masks the polarization signature of the buried terrain. In addition, if

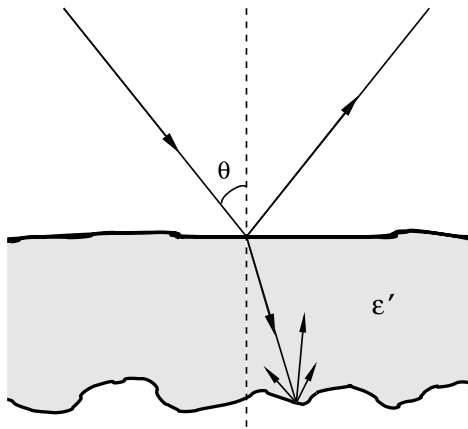


**Figure 4.** A wave is incident on a mantled surface at incidence angle  $\theta$ , is refracted at an angle determined by the dielectric constant  $\epsilon'$ , and reflects from a rough substrate.

the subsurface interface is between two materials with similar dielectric constants, or if the dielectric constant changes gradually with depth, there will not be a significant interface and the subsurface reflectivity will be small.

[20] Attenuation of the radar wave by the surface layer can also effect the observed degree of linear polarization. The loss tangent ( $\epsilon''/\epsilon'$ ) of the Venus surface is not well known, but typical values for terrestrial materials range from 0.001–0.1 for volcanic rocks with a range of densities [Campbell and Ulrichs, 1969]. At the low-loss end of this range, we could possibly detect reflections from a surface layer with thickness of up to 20 meters (for the 12.6 cm radar wave). For loss tangents of 0.01, the penetration depth is on the order of 1–2 m.

[21] Finally, spatial averaging over a large area with a few small local layered regions will produce a lower degree of linear polarization. If only part of the area is mantled and gives a subsurface reflection, then  $S_1$  will be enhanced relative to  $S_2$  and  $S_3$ , leading to a smaller value of  $m_l$ . The large number of unknowns—surface and subsurface dielectric constant, loss tangent, depth to the reflecting surface, surface roughness, and the fraction of mantled surface per pixel—make it difficult to model the scattering and derive quantitative estimates of these physical parameters. However, the data can still be interpreted in a qualitative way.

[22] A terrestrial example can help illustrate the use of the degree of linear polarization maps. The NASA/JPL AIRSAR system collects the full Stokes scattering operator for each image pixel at wavelengths of 5.7, 24, and 68 cm. Figure 6a shows a C band (5.7 cm wavelength) AIRSAR image of the Stovepipe Wells region of Death Valley, CA. The valley is flanked by mountains that have extensive fans of associated alluvial debris. Intermittent discharge of water and sediment onto these fans creates digitate deposits of fine material that cover the rocky surface. On the valley floor, dune fields surround a relatively flat region of sand mantle over cracked mud layers (Figure 7). The sand mantle is about 5–10 cm deep, whereas in the dune fields the sand covering ranges from a few centimeters to the full depth of the dunes

(about three meters). Figure 6b shows a color overlay map of the linear-polarized component for the area covered in Figure 6a. The linear-polarized echo component is very low in areas that have significant surface roughness at the scale of the radar wavelength (e.g., the mountains and rocky portions of the alluvial fans). The highest values of the degree of linear polarization are found for the sand-mantled areas, flat-interdune patches, and areas of recent fine sediment deposition on the fans. The degree of linear polarization values for the sand mantled area vary somewhat, but are usually around 0.5. The linear component associated with the dune fields probably comes from thin patchy coverage of the hard-packed base between the big dunes.

[23] In areas with moderate to high degree of linear polarization, the polarization angle is typically close to  $\pm 90^\circ$ , indicating a predominately vertically polarized component. There is also a strong inverse correlation between the fraction of linear polarization and the HH/VV ratio. Both behaviors are consistent with the expected effect of the Fresnel transmission coefficients, which favor V-polarized incident energy, on signals transmitted through a dielectric interface [Campbell, 2002]. On the basis of these results, we conclude that the strong linearly polarized returns observed are due to radar reflections from surfaces mantled by dry sand or fine debris. The incidence angle is  $64^\circ$  at the bottom of the images and  $31^\circ$  at the top, and is about  $54^\circ$  at the field location shown in Figure 7. There is not a gradient in linear polarization with incidence angle, probably because the

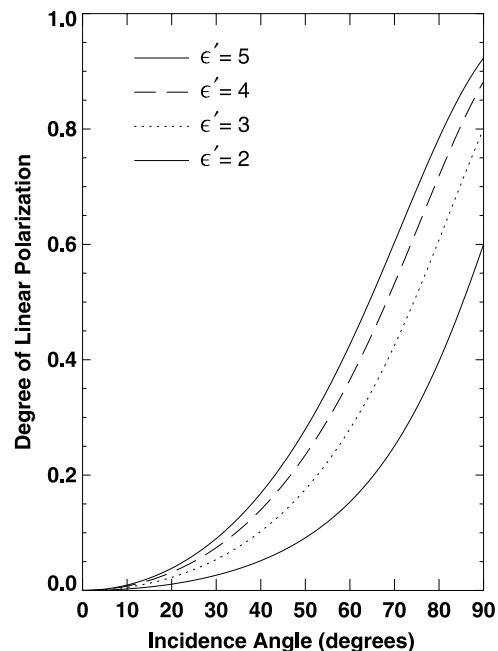


**Figure 5.** Graph of the relationships between incidence angle ( $\theta$ ), surface dielectric constant ( $\epsilon'$ ), and degree of linear polarization ( $m_l$ ) for a wave that is transmitted into a mantling deposit and reflects from a gently undulating subsurface structure.

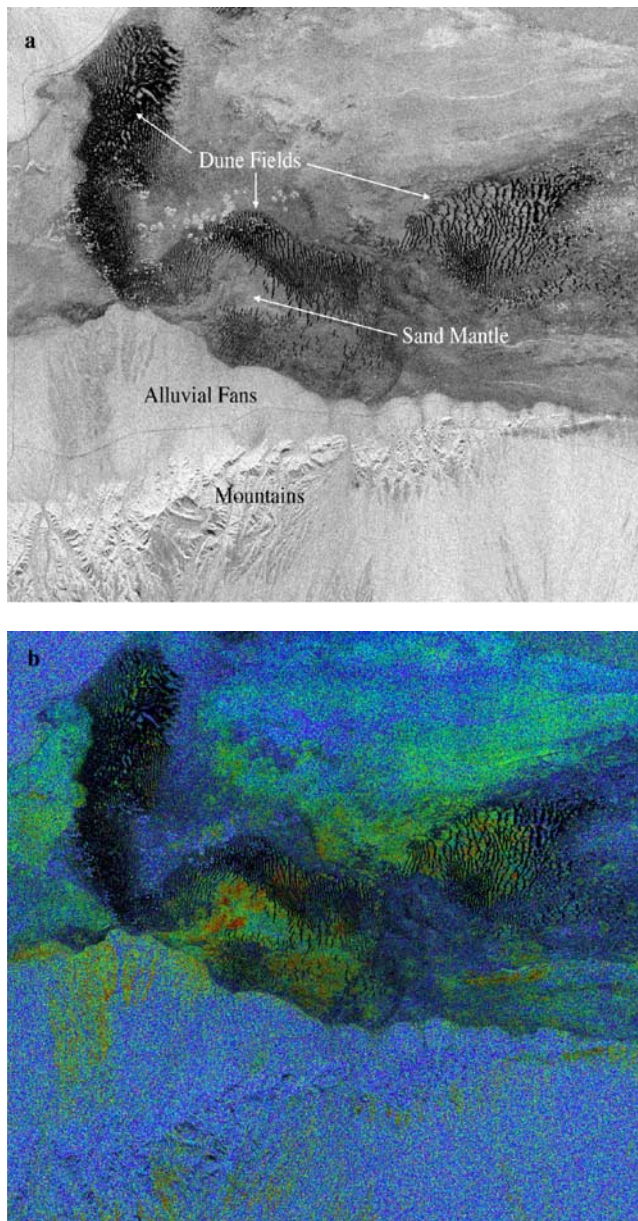


**Figure 6.** (a) C band (5.7 cm) radar image of the Stovepipe Wells region of Death Valley, California. Horizontal image width is  $\sim 13.5$  km; the vertical dimension is a slant range projection, with a range pixel length of  $\sim 6.7$  m and a total range extent of  $\sim 8.1$  km. The radar polarization was left-circular transmit and right-circular receive (LR). The radar flight line is across the top of the image; incidence angle increases toward the bottom. The location from which the photo shown in Figure 7 was taken is at the tip of the arrow for the “Sand Mantle” area. (b) Color overlay of the linearly polarized fraction of returned radar echo for the area shown in Figure 6a. Red indicates fractions of  $\sim 50\%$ , green indicates fractions of  $\sim 25\text{--}40\%$ , and blue is  $0\%$ . Note that the linearly polarized echo is near zero in rough areas (e.g., mountains and rocky portions of fans) and is highest where the surface is covered by a sand mantle or recently deposited fine sediment.

percent linear polarization for each pixel depends more on the character and distribution of the mantling layer than on the incidence angle.

#### 4. Regional Variation in the Degree of Linear Polarization

[24] Figure 2 shows an example of our degree of linear polarization data compared to a total power image of the surface and a Magellan SAR image mosaic. The Mercator projection maps of the Arecibo data show the northern hemisphere results from 2001. Note that the region near the subradar point ( $0^\circ$  incidence angle) has a degree of linear polarization close to zero, and the value of  $m_l$  increases with incidence angle. In addition, areas with a high degree of linear polarization do not necessarily correspond to the regions with the highest total backscatter. Both of these effects indicate a very low degree of instrumentally induced linear polarization. The degree of linear polarization map shows numerous “features” which typically have a fractional linear polarization between 0.10 and 0.35. The lower resolution used in 2001 and improvements to the Arecibo telescope led to much better signal-to-noise than in 1999. This is especially noticeable at high incidence angles, and it means that linear polarization features can be observed over a larger latitude-longitude range in the 2001 data set.

[25] The degree of linear polarization maps correlate very well with terrain units in the Magellan SAR images, and specific linear polarization features line up exactly with volcanic dome fields, areas of wind streaks, and impact crater surroundings. It is clear that there are large regions where the 12.6 cm radar wave penetrates into the surface and reflects from either a subsurface layer or from buried rocks. The degree of linear polarization features in our maps occur mostly in plains regions. Impact crater ejecta blankets,

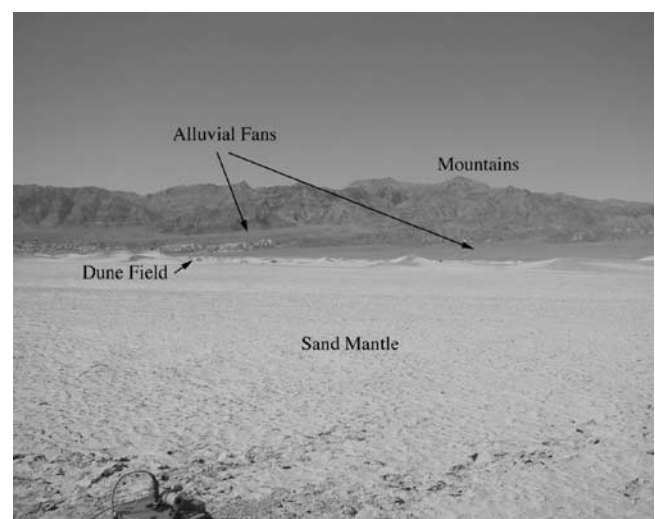


**Figure 7.** Photo of Death Valley, looking from the Valley floor toward the mountains (at the bottom of Figure 6a). For a sense of scale, the radar equipment in the left foreground is about 30 cm across and the dunes in the background are 2–3 m high.

tessera terrain, and other mountainous areas typically show no linear polarization, although in a few cases enhanced linear polarization appears close to larger volcanic structures such as Beta Regio.

[26] It was possible to compare a few of the degree of linear polarization features that were visible in both years of Arecibo observations. Since the subradar point changed between epochs, the incidence angle to specific features also changed. Many features visible in one year are not visible in the other because the incidence angle at one epoch is either too high to have adequate signal-to-noise, or too low to have any significant degree of linear polarization. However, the features that we could compare have a similar spatial structure in both epochs. For a given feature, the value of  $m_l$  should change between epochs as the incidence angle changes. The amount of change expected depends on the specific scattering model and on the two different incidence angles. For an incidence angle change of  $15^\circ$  at mid-latitudes, the value of  $m_l$  should change by  $\sim 0.1$ , which is only slightly larger than the errors in  $m_l$  discussed in section 2. About half of the features visible in both years of data show a small (less than 0.1) increase in  $m_l$  with increasing incidence angle, but the other half show no change in the degree of linear polarization. Errors in the value of  $m_l$  and differences in the amount of spatial averaging between the two years make it almost impossible to accurately measure small changes in  $m_l$  from one year to the next.

[27] We also checked the behavior of the polarization angle ( $\chi$ ), which should rotate as the plane of incidence changes across the surface of the planet. The calculated polarization angles are not calibrated, but we do observe a trend in  $\chi$  with observing geometry that is consistent with subsurface echoes. In particular, none of the degree of linear polarization features have a polarization angle that deviates significantly from this trend, which is evidence that the features are produced by the same physical mechanism, most likely subsurface scattering.

[28] The Venera landers took optical images of the surface, which gives us the opportunity to compare the linear polarization results with ground truth observations. Most of the landing sites are too close to the equator or to the subradar point to be visible in our data [Colin, 1983]; however, the Venera 9 and Venera 10 sites fall within the usable incidence angle range. Venera 9 landed at a rocky site, while Venera 10 images revealed a site with more regolith exposed at the surface [Florenskiy *et al.*, 1983]. The linear polarization measurements for the sites are 0.09 at the Venera 9 site and 0.05 at the Venera 10 site, and averages of  $m_l$  over a 300 km square box surrounding the landing sites are 0.09 and 0.07, respectively. These values are smaller than those associated with any of the crater sites at similar incidence angles. This indicates that the patchy surface covering present near the landing sites is not adequate to produce the values of  $m_l$  associated with our crater sites.

## 5. Geologic Interpretation for Impact Crater Deposits

[29] A large fraction of the most distinctive degree of linear polarization features in the Arecibo maps are associated with impact craters. The craters and their locations

are shown in Table 1. There are 17 craters that have a convincing connection with a strong linearly polarized echo feature, and 28 additional craters where the association is ambiguous. A linear polarization feature is considered to have a definite association with a crater if the feature surrounds the crater or closely matches crater-related deposits, such as a halo or parabola. The association is considered ambiguous if the crater lies close to a large volcano or volcanic dome field, or if the degree of linear polarization feature is close to a crater but is not clearly matched to anything visible in the SAR images. Some of these uncertain cases may be deposits related to the crater, but others may be areas of aeolian deposition or volcanism, so they were not considered to have a definite association with the crater. The degree of linear polarization features are generally asymmetric with respect to the crater center, and usually lie to the western side of the crater or form a partial ring around the crater. The degree of linear polarization is always close to zero on the craters and their radar-bright ejecta blankets, with the exception of Stuart, where a high degree of linear polarization, as well as an anomalously low emissivity (0.69), are associated with the 67 km diameter floor [D. B. Campbell *et al.*, 1992].

[30] Overlays for craters with the most interesting linear polarization correlations are shown in Figure 3. Each image has been stretched to a color scale individually in order to provide the clearest display for each feature. Note that the degree of linear polarization varies across individual features, and the maximum value of the degree of linear polarization changes from feature to feature. As explained in section 3, the large number of variables contributing to linear polarization value make it difficult to unambiguously model the physical parameters (such as dielectric constant) of the deposits. However, the overlays can still be interpreted in a qualitative way.

[31] Although changes in dielectric constant can contribute to differences in  $m_l$ , it seems unlikely that changes in the degree of linear polarization across a given feature are caused primarily by spatial variation in the dielectric constant of the mantling layer, especially in cases where the high  $m_l$  values cover an area of consistent Magellan backscatter cross section. It seems more plausible that most changes in the degree of linear polarization across individual features are caused by the spatial coverage effect or by differences in deposit thickness. The brightest areas in our linear polarization maps (the red areas in the overlays) may represent areas where the surface cover is more ubiquitous, while the areas with intermediate values (green in the overlays) have larger fractions of the resolution cell with no strong subsurface echoes.

### 5.1. Correlations Between $m_l$ and Magellan SAR and Emissivity Data

[32] Studying the crater overlays reveals that the regions with the highest degree of linear polarization are usually areas where the SAR imagery shows an amorphous area of slightly higher cross section. This can be seen in many of the SAR images shown in Figure 3, but Anya, Carson, Xantippe, and Nelike (shown in Figures 3a, 3d, 3e, and 3f) are good examples. These brighter patches have a relatively featureless appearance and the “underlying” terrain appears muted but is usually still visible. These radar-bright patches

**Table 1.** Craters With Nearby Linearly Polarized Echo Component

Crater Name <sup>a</sup>	Latitude <sup>b</sup>	Longitude	Location of Linear Polarization With Respect to Crater
Bahriyat	50.3°N	357.5°E	northeast of the crater
GALINA	47.6°N	307.1°E	on dark halo surrounding the crater
Ruth	43.3°N	19.9°E	southwest of the crater
Zina	42.0°N	320.0°E	surrounding the crater
Jeanne	40.1°N	331.5°E	primarily south and east of the crater
ANYA	40.0°N	295.6°E	west of the crater
de Stael	37.4°N	324.2°E	south, east, and west of the crater
Wilma	36.7°N	1.7°E	west of the crater
Vassi	34.4°N	346.5°E	surrounding the crater
WAZATA	33.6°N	298.3°E	west of the crater
Noreen	33.6°N	22.7°E	patches east, west, and south of the crater, close to Edgeworth
Al-Taymuriyya	32.9°N	336.2°E	surrounding the crater
Edgeworth	32.2°N	22.8°E	patches south, northeast, and northwest of the crater, by Noreen
Saida	28.2°N	302.0°E	west of the crater
BARTON	27.4°N	337.5°E	ring shape surrounds both this crater and Lachapella
LACHAPELLE	26.7°N	336.7°E	ring shape surrounds both this crater and Barton
ROXANNA	26.5°N	334.6°E	surrounded by the ring-shaped feature around Barton
WEST	26.1°N	303.0°E	southeast of the crater
LILLIAN	25.6°N	336.0°E	surrounded by the ring-shaped feature around Barton
Audrey	23.8°N	348.1°E	surrounding the crater
Heidi	23.6°N	350.1°E	surrounding the crater
Veriko	20.4°N	350.1°E	surrounding the crater
AURELIA	20.3°N	331.8°E	in a rough parabola, following the SAR parabola
WEIL	19.3°N	283.1°E	surrounding crater, but mostly to the southeast
SHIH MAI-YU	18.4°N	318.9°E	on dark halo surrounding crater
Domnika	18.4°N	294.3°E	north and east of crater
Vasilutsa	16.5°N	334.4°E	east of crater
Cunitz	14.5°N	350.9°E	surrounding the crater on a radar-bright halo
Rhys	8.6°N	298.8°E	surrounding the crater, near Boivin
Khafiza	6.0°N	299.2°E	surrounding the crater, near Boivin
Dyasya	5.1°N	297.6°E	surrounding the crater, near Boivin
BOIVIN	4.2°N	299.5°E	surrounding the crater, U-shaped west of the crater
Madeleine	4.8°S	293.2°E	surrounding crater, but stops abruptly southeast of crater
XANTIPPE	10.9°S	11.7°E	mostly northeast of the crater
Leslie	11.2°S	13.5°E	surrounded by the Xantippe feature
Scarpellini	23.3°S	34.6°E	surrounding the crater
CARSON	24.2°S	344.1°E	in a rough parabola shape corresponding to bright SAR areas
Danilova	26.4°S	337.2°E	surrounding the crater
Aglaonice	26.5°S	240.0°E	east of the crater
NELIKE	26.8°S	329.2°E	in a parabola shape to the west of the crater
Saskia	28.6°S	337.1°E	surrounding the crater
STUART	30.8°S	20.2°E	on the crater floor
Dix	37.0°S	329.0°E	surrounding the crater
Polenova	45.5°S	335.5°E	surrounding the crater
NYOGARI	46.5°S	306.4°E	southwest of crater

<sup>a</sup>Craters in all capital letters have a definite association with a linear polarization feature.

<sup>b</sup>Locations taken from *Herrick et al.* [1997] online database.

near craters were previously interpreted either as places where scouring by impact-generated winds blew away fine material leaving centimeter sized rocks on the surface, or as areas of microdunes [Schaller and Melosh, 1998; Weitz *et al.*, 1994]. Since the data shows surface penetration of the wave, these areas cannot be simply rough basements that were completely stripped of a surface layer. The higher backscatter cross section has to be explained without invoking a strong surface reflection from wavelength scale roughness. Scattering from a rough, mantled subsurface or buried rocks could create a high radar backscatter and enhanced values of  $m_l$ . Another possibility is that the surface is only partially mantled, and the smoother mantled regions between patches of rough surface lead to high  $m_l$  values. The power backscattered from the subsurface may also be larger than that expected from a non-mantled surface, because the angle of incidence onto the subsurface is increased by refraction at the surface-atmosphere bound-

ary. The magnitude of the increase depends strongly on deposit depth and loss tangent, but for loss tangents of 0.01 the reflection from a mantled surface could be larger than the corresponding reflection from the non-mantled surface for deposits that are several tens of centimeters thick.

[33] Many of the degree of linear polarization features fully or partially overlap low emissivity features mapped by the Magellan radiometer. In plains regions on Venus, areas of lower emissivity are frequently close to impact craters, and *Lawson and Plaut* [1994] suggest that impact events are the major cause of low emissivity in the plains. These lower emissivity patches typically have values greater than 0.75 but less than the average emissivity of 0.84 [Pettengill *et al.*, 1992]. The low emissivity has been attributed to an enhanced dielectric constant [Pettengill *et al.*, 1992; *Lawson and Plaut*, 1994], although there have been suggestions that it may

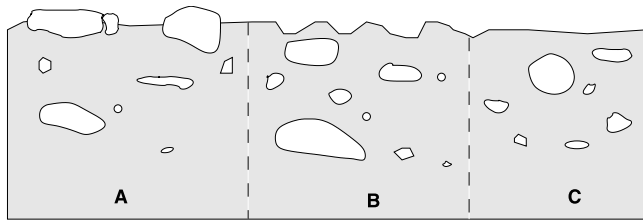


**Figure 8.** A sketch of scenarios that can produce the enhanced linear echo polarization. Section A shows a mantled surface with rocks exposed at the surface. The linearly polarized echo component would be produced by the portions of the incident radar wave that were able to penetrate into the surface between the rocks. Section B shows a mantling layer that has been roughened at the surface. Section C shows a smooth, surficial deposit that covers buried rocks. In all cases, the subsurface reflection could come from either buried rocks, as is shown here, or from a buried substrate.

be due to volume scattering from rocks in a low-loss medium [Tryka and Muhleman, 1992]. In some cases the correspondence between  $m_l$  and emissivity is quite striking; for example, the spatial structure of the enhanced linear polarization around Carson closely matches the shape of the low-emissivity region surrounding the crater. Other craters with overlapping linear polarization and low-emissivity areas are Anya, Ruth, Wilma, Noreen, and Xantippe. Stuart crater (Figure 2g) has one of the lowest emissivity crater floors, and the degree of linear polarization maps also show a strong linearly polarized echo component from the floor. Many other craters show very slight ( $\sim 0.01$ – $0.02$ ) emissivity decreases over part of our degree of linear polarization feature, for example Barton, Aurelia, and Shih Mai-Yu. However, some craters that have low emissivity surroundings do not show linearly polarized enhancements; for example, an area near the crater Bender, and the Faustina and Stuart parabolas, have emissivities lower than the average plains values but show no linear polarization enhancement.

[34] Our analysis shows a clear connection between diffuse, slightly higher backscatter cross section, lower emissivity, and linear polarization enhancement near impact craters. One possible explanation is that the linear polarization comes from regions where the surface is smooth, such that the emissivity measured by Magellan is actually the true H-polarized emissivity, which is lower than the emissivity of a rough surface [Pettengill *et al.*, 1992]. The emissivity of rough surfaces tends toward the average of the individual emissivities for the horizontal and vertical polarizations [Campbell, 1994], and it is larger than the H-polarized emissivity at the incidence angles of the Magellan data. In most cases the emissivity of the linear polarization features is only 0.01–0.04 below average plains values, which can be explained by this difference in roughness, but the emissivity of the high- $m_l$  feature near Xantippe is 0.72, and the emissivity of the floor of Stuart crater is 0.69. It is difficult to explain such low emissivities solely through roughness changes. If the surfaces of the deposits with enhanced  $m_l$  are very smooth, then the higher

backscatter cross section must arise from scattering by buried rocks or by a rough substrate.

## 5.2. Possible Scenarios for Producing High $m_l$ Values

[35] There are several scenarios in which a mantling layer could form that would produce a strong, linearly polarized echo component in regions near impact craters. These include: topographic depressions that confine dust and debris; smooth, mantled surfaces overlying buried rocks; microdune fields or ripples over a rough substrate; and parabola deposits.

### 5.2.1. Topographically Trapped Dust and Debris

[36] Comparing the degree of linear polarization data with Magellan topography reveals some cases where a high value of  $m_l$  correlates with depressions surrounded by elevated terrain such as deformation belts or tesserae. These might represent “traps” for crater-related debris or wind-blown fines from other sources. The clearest example is the feature that surrounds Barton, Lachappelle and two smaller craters (Figure 3b). The degree of linear polarization feature is nearly circular and overlies a topographic low surrounding the craters. The area with the highest degree of linear polarization corresponds to a diffuse radar-bright ring in the SAR images. For other craters, the linear polarization is only partially bounded by topographic highs. The craters Wilma and Galina are good examples. Galina is partially surrounded by elevated terrain to the north and west, while the deposit near the crater Wilma is bounded on the south, east, and west sides.

### 5.2.2. Blocks or a Substrate Buried Under Fine Crater Ejecta

[37] For some of the high- $m_l$  features, it is possible that the surface is fairly smooth, and the degree of linear polarization is caused by reflections from large pieces of buried impact ejecta (Figure 8c). A possible analogy is a radar bright halo seen around one of the craters imaged with the SRL [McHone *et al.*, 2002]. Radar images of the crater show a diffuse, bright halo that extends about 1 km from the rim; however, the halo region is sand-covered. McHone *et al.* [2002] suggest that the radar is penetrating the mantling sand layer and reflecting off blocks of impact ejecta that are completely buried. If this is happening on Venus, it would indicate that some radar bright regions in the Magellan SAR images may have relatively smooth surface layers. Although most of the high- $m_l$  features correlate with bright areas in the SAR images, we also see a high value of  $m_l$  from some radar-dark regions, like the dark halos surrounding the craters Galina and Shih Mai-Yu. In this case the linear polarization must arise from subsurface reflections from beneath a very smooth surface layer.

### 5.2.3. Partially Mantled Surfaces, Ripples, or Dunes

[38] Another alternative for cases where there is a correlation between high  $m_l$  values and radar-bright terrain is that the surface is rough, but not so rough that the polarization signature is totally randomized. For example, rough, radar bright regions near craters may have been formed when a surface coating was partially, but not completely, scoured out by wind. In this case, the degree of linear polarization would be coming from patches of covered terrain between partially exhumed regions of the surface. The surface might be mostly smooth and mantled, but have embedded rocks (Figure 8a).

[39] The bright patches could also be areas of microdunes or ripples that overlie a subsurface layer or buried rocks (Figure 8b). Laboratory experiments have shown that sand sized particles are easily moved by winds on Venus and can form ripples [Greeley *et al.*, 1984; Marshall and Greeley, 1992]. Weitz *et al.* [1994] compared the left-looking and right-looking Magellan data and discovered that both Guan Daosheng and Eudocia have a radar bright parabola in the left-looking images that disappears when viewed from the right. These changes in radar brightness with look direction are attributed to small, unresolved dunes or ripples with a wavelength of order 10 cm [Weitz *et al.*, 1994].

#### 5.2.4. Parabola Deposits

[40] The degree of linear polarization data also show high values of  $m_l$  from the parabolas surrounding the craters Aurelia, Carson, and Neline (shown in Figures 3a, 3c, and 3f), as well as from one of the large dark circular features (Galina) identified by *D. B. Campbell et al.* [1992]. There is also a linearly polarized echo component near the craters Ruth and Noreen, however in these cases the degree of linear polarization feature does not closely match the deposit shapes visible in the SAR images so the connection is less certain.

[41] Neline and Aurelia have high- $m_l$  features that closely match the parabolas seen in the SAR images. Figure 3f shows the degree of linear polarization for the region surrounding the crater Neline (6.1 km), which is located just east of Ushas Mons. Neline was not previously classified as a crater with a parabolic deposit [*D. B. Campbell et al.*, 1992; Schaller and Melosh, 1998], but it has a dark parabola and an inner bright parabola in the Magellan SAR images. The area with the highest degree of linear polarization overlies the outer margin of Neline's parabolic deposit. The Aurelia parabola (Figure 3c) also has high  $m_l$  values around the outer edge and low values in the interior.

[42] Other parabolas have an associated linearly polarized echo feature, but not in the typical parabola shape. Carson crater is one of the more unusual parabola craters. It has a bright deposit west of the crater, as well as a small bright parabolic arc just east of the crater. The high- $m_l$  feature corresponds to the higher cross-section areas just west and east of the crater, while the radar dark bands on either side of the bright deposits show a smaller degree of linear polarization. The linear polarization signature crosses a deformation band to the west of the crater, so either the deformation band is exposed at the surface, or the mantling layer is thin enough to allow the radar wave to easily penetrate and reveal subsurface structure. Many of the degree of linear polarization features overlie fractures or deformation bands; other examples are Noreen, Aurelia and Xantippe.

[43] If the higher degree of linear polarization corresponds to areas where there is a more uniform surface coating, it should be possible to compare our data with the distribution of ejecta predicted by parabola formation models. *Vervack and Melosh* [1992] model the formation of parabolas for cases where the vapor plume produced by the impact breaches the atmosphere, which is estimated to happen for craters with diameters larger than about 20 kilometers. *Schaller and Melosh* [1998] fit this model to the parabolas and dark halos listed by *D. B. Campbell et al.* [1992], and their results show that the parabolas typically

have an average thickness of 2–20 cm, where the average thickness is defined as the total volume of material divided by the total area of the parabola. The thickness of the deposits at the outer edge of the observable dark parabola is usually around one cm, which is consistent with *D. B. Campbell et al.* [1992], who estimated that the minimum deposit thickness needed to see a parabola with the Magellan radar is about two centimeters. According to the model, the thickness of the parabola deposit is graded, with the thickest areas near the source crater. In addition, the larger (1–5 cm) sized particles land close to the crater and end up underneath finer particles which settle more slowly out of the atmosphere and can travel farther.

[44] The *Schaller and Melosh* [1998] models predict a deeper coating in the middle of the parabola with thinner layers at the edges. If the central portions of Neline and Aurelia show a lower degree of linear polarization because they have less surface coverage, then the *Schaller and Melosh* [1998] model of parabola formation does not accurately describe these observations. It is possible that these parabolas have been modified since their formation and the high  $m_l$  values on the outer edges are relatively undisturbed portions of the deposit. Alternatively, the inner regions of the parabolas might produce negligible values of  $m_l$  because the deposits are thicker in the center and the radar wave is attenuated. If there is a thick mantling layer covering the parabola interiors, one might expect that the SAR images would show fewer structures there. However, fractures are visible throughout the Aurelia parabola and do not disappear toward the center. Either the deposit is thick and the fractures are large enough to be present at the surface, or the surficial layer in this region is thin but too patchy to show a high degree of linear polarization. All five of the parabolas that have a strong linearly polarized echo component in the Arecibo data show some type of fractures or deformation that continues through the central areas.

## 6. Discussion and Conclusions

[45] The degree of linear polarization maps show that many areas on Venus are covered by a surficial layer that is transparent to the 12.6 cm radar wave. Linearly polarized echoes are found near 45 impact craters, including a few of the parabola deposits, and it is most likely that these areas are covered by surface layers that are centimeters to several tens of centimeters in depth. In general, the highest degree of linear polarization comes from areas with a slightly higher backscatter cross section. This enhanced radar brightness could be produced by reflections from a mantled rough substrate or from rocks in or on the mantling layer itself. In addition, areas with high  $m_l$  values tend to correspond to low emissivity areas. In most cases this can be explained by changes in surface roughness, but in at least two cases the emissivity is lower than might be expected for such a mechanism.

[46] It is interesting that there is not a strong linearly polarized echo component associated with most of the parabolic deposits in our viewing range. There are 13 parabolas and 4 large dark circular features that fall within the latitude/longitude range of the Arecibo observations and are far enough away from the subradar point that they could show a high degree of linear polarization, but only a small

fraction of them appear as features in our data. For example, the crater Faustina has an associated dark parabolic deposit that partially mantles a bright lava flow [D. B. Campbell *et al.*, 1992]. Modeling the Faustina parabola using a two-layer model gives deposit depths from 1–2 meters [D. B. Campbell *et al.*, 1992]. However, our maps show no evidence of the parabola, despite an incidence angle of almost 45° in the 2001 data set. We also do not see the large dark parabola associated with the crater Stuart.

[47] It is clear that the conditions needed to produce a linearly polarized echo component are not met for most parabolas, but it is difficult to ascertain which specific condition is responsible. One possibility is that the dark parabolas are thick enough to attenuate the transmitted wave almost completely. For instance, perhaps the parabolas start out as deep deposits and are later thinned by wind erosion. Most of the dark parabolas overlie radar-bright geologic features, such as fractures, and if the surface layer is thick enough to prevent subsurface reflections, then these bright reflecting structures must be present at the surface. In addition, parabola formation models predict that the edges of the parabolas should be 1–2 cm thick [Schaller and Melosh, 1998], so we should at least see linear polarization from the outer portions of the deposit, unless the thinner parts cover such a small area that they are not visible at our resolution.

[48] A second possible explanation is that the dark parabolas do not have a sharp dielectric boundary that can reflect a significant amount of power. For example, the porosity and dielectric constant may change more gradually through the deposit, or there may simply be a lack of large buried rocks available to return an echo from the subsurface.

[49] The wide spatial distribution of linearly polarized echoes over the plains of Venus suggests that there may be much more fine-grained mantling material than previously determined from analysis of Magellan images. In addition to the crater-related deposits, the degree of linear polarization maps show mantling layers on some dome fields and on the flanks of some of the large volcanoes. Further work on these volcano-related features is currently in progress. Radar observations at 70 cm wavelength may also help constrain the scattering mechanisms that produce the linearly polarized echoes.

[50] **Acknowledgments.** We gratefully acknowledge assistance from A. Hine, M. Nolan, P. Perillat, and the Arecibo Observatory staff. L. Carter, D. Campbell, and B. Campbell are partially supported under grants through NASA's Planetary Geology and Geophysics Program. L. Carter was also supported by a National Science Foundation Graduate Research Fellowship. Arecibo Observatory is part of the National Astronomy and Ionosphere Center, which is operated by Cornell University under cooperative agreement with the NSF and with support from NASA.

## References

- Basilevsky, A. T., and J. W. Head (2002), Venus: Analysis of the degree of impact crater deposit degradation and assessment of its use for dating geological units and features, *J. Geophys. Res.*, *107*, 5061, doi:10.1029/2001JE001584.
- Campbell, B. A. (1994), Merging Magellan emissivity and SAR data for analysis of Venus surface dielectric properties, *Icarus*, *112*, 187–203.
- Campbell, B. A. (2002), *Radar Remote Sensing of Planetary Surfaces*, Cambridge Univ. Press, New York.
- Campbell, B. A., S. H. Zisk, and P. J. Mougini-Mark (1988), Lunar surface scattering from new 3-cm polarization and phase radar data (abstract), *Lunar Planet. Sci.*, *XIX*, 161.
- Campbell, B. A., J. F. Bell III, S. H. Zisk, B. R. Hawke, and K. A. Horton (1992), A high-resolution radar and CCD imaging study of crater rays in Mare Serenitatis and Mare Nectaris, *Proc. Lunar Planet. Sci. Conf. 22nd*, 259–274.
- Campbell, D. B., N. J. S. Stacy, W. I. Newman, R. E. Arvidson, E. M. Jones, G. S. Musser, A. Y. Roper, and C. Schaller (1992), Magellan observations of extended impact crater related features on the surface of Venus, *J. Geophys. Res.*, *97*, 16,249–16,277.
- Campbell, M. J., and J. Ulrichs (1969), Electrical properties of rocks and their significance for lunar radar observations, *J. Geophys. Res.*, *74*, 5867–5881.
- Colin, L. (1983), Basic facts about Venus, in *Venus*, edited by P. M. Hunten *et al.*, pp. 10–26, Univ. of Ariz. Press, Tucson.
- Florenskiy, K. P., A. T. Bazilevsky, C. A. Burba, O. V. Nicolayeva, A. A. Pronin, A. S. Selivanov, M. K. Narayeva, A. S. Panfilov, and V. P. Chemondanov (1983), Panorama of Venera 9 and 10 landing sites, in *Venus*, edited by P. M. Hunten *et al.*, pp. 137–153, Univ. of Ariz. Press, Tucson.
- Greeley, R., J. Iversen, R. Leach, J. Marshall, B. White, and S. Williams (1984), Windblown sand on Venus: Preliminary results from laboratory simulations, *Icarus*, *57*, 112–124.
- Hagfors, T., and D. B. Campbell (1974), Radar backscattering from Venus at oblique incidence at a wavelength of 70 cm, *Astron. J.*, *79*, 493–502.
- Hagfors, T., and J. V. Evans (1968), Radar studies of the Moon, in *Radar Astronomy*, edited by J. V. Evans and T. Hagfors, chap. 5, pp. 219–273, McGraw-Hill, New York.
- Herrick, R. R., V. L. Sharpton, M. C. Malin, S. N. Lyons, and K. Feely (1997), Morphology and morphometry of impact craters, in *Venus II*, edited by S. W. Bougher, D. M. Hunten, and R. J. Phillips, pp. 1015–1046, Univ. of Ariz. Press, Tucson.
- Izenberg, N. R., R. E. Arvidson, and R. J. Phillips (1994), Impact crater degradation on Venusian plains, *Geophys. Res. Lett.*, *21*, 289–292.
- Jackson, J. D. (1999), *Classical Electrodynamics*, 3rd ed., John Wiley, Hoboken, N. J.
- Lawson, S. L., and J. J. Plaut (1994), Impact related low-emissivity anomalies on Venus (abstract), *Lunar Planet. Sci.*, *XXV*, 781–782.
- Marshall, J. R., and R. Greeley (1992), An experimental study of aeolian structures on Venus, *J. Geophys. Res.*, *97*, 1007–1016.
- McHone, J. F., R. Greeley, K. K. Williams, D. G. Blumberg, and R. O. Kuzmin (2002), Space shuttle observations of terrestrial impact structures using SIR-C and X-SAR radars, *Meteorit. Planet. Sci.*, *37*, 407–420.
- McKinnon, W. B., K. J. Zahnle, B. A. Ivanov, and H. J. Melosh (1997), Cratering on Venus: Models and observations, in *Venus II*, edited by S. W. Bougher, D. M. Hunten, and R. J. Phillips, pp. 969–1014, Univ. of Ariz. Press, Tucson.
- Pettengill, G. H., P. G. Ford, and R. J. Wilt (1992), Venus radiothermal emission as observed by Magellan, *J. Geophys. Res.*, *97*, 13,091–13,102.
- Phillips, R. J., R. F. Raubertas, R. E. Arvidson, I. C. Sarkar, R. H. Herrick, N. Izenberg, and R. E. Grimm (1992), Impact craters and Venus resurfacing history, *J. Geophys. Res.*, *97*, 15,923–15,948.
- Schaber, G. G., R. G. Strom, H. J. Moore, L. A. Soderblom, R. L. Kirk, D. J. Chadwick, D. D. Dawson, R. L. Gaddis, J. M. Boyce, and J. Russell (1992), Geology and distribution of impact features on Venus: What are they telling us?, *J. Geophys. Res.*, *97*, 13,257–13,301.
- Schaller, C. J., and H. J. Melosh (1998), Venusian ejecta parabolas: Comparing theory with observations, *Icarus*, *131*, 123–137.
- Schultz, P. (1992), Atmospheric effects on ejecta emplacement and crater formation on Venus from Magellan, *J. Geophys. Res.*, *97*, 16,183–16,248.
- Stacy, N. J. S. (1993), High-resolution synthetic aperture radar observations of the Moon, Ph.D. thesis, Cornell Univ., Ithaca, N. Y.
- Tryka, K. A., and D. O. Muhleman (1992), Reflection and emission properties on Venus: Alpha Regio, *J. Geophys. Res.*, *97*, 13,379–13,394.
- Vervack, R. J., Jr., and H. J. Melosh (1992), Wind interaction with falling ejecta: Origin of the parabolic features on Venus, *Geophys. Res. Lett.*, *19*, 525–528.
- Weitz, C. M., J. J. Plaut, R. Greeley, and R. S. Saunders (1994), Dunes and microdunes on Venus: Why were so few found in the Magellan data?, *Icarus*, *112*, 282–295.

B. A. Campbell, Center for Earth and Planetary Studies, National Air and Space Museum, Smithsonian Institution, MRC 315, Room 3785, Washington, DC 20560, USA. (campbellb@nasm.si.edu)  
 D. B. Campbell and L. M. Carter, Department of Astronomy, Cornell University, Space Sciences Building, Ithaca, NY 14853, USA. (lcarter@astro.cornell.edu)